

Interleaved Atom Interferometry for High Sensitivity Inertial Measurements

D. Savoie[†], M. Altorio[†], B. Fang, L. A. Sidorenkov, R. Geiger^{*}, A. Landragin

LNE-SYRTE, Observatoire de Paris, Université PSL, CNRS, Sorbonne Université
61 Avenue de l'Observatoire, 75014 Paris, France

[†]These authors contributed equally to this work.

^{*}To whom correspondence should be addressed; E-mail: remi.geiger@obspm.fr.

Cold-atom inertial sensors target several applications in navigation, geoscience and tests of fundamental physics. Reaching high sampling rates and high inertial sensitivities, obtained with long interrogation times, represents a challenge for these applications. We report on the interleaved operation of a cold-atom gyroscope, where 3 atomic clouds are interrogated simultaneously in an atom interferometer featuring a 3.75 Hz sampling rate and an interrogation time of 801 ms. Interleaving improves the inertial sensitivity by efficiently averaging vibration noise, and allows us to perform dynamic rotation measurements in a so-far unexplored range. We demonstrate a stability of 3×10^{-10} rad.s⁻¹, which competes with the best stability levels obtained with fiber-optics gyroscopes. Our work validates interleaving as a key concept for future atom-interferometry sensors probing time-varying signals, as in on-board navigation and gravity-gradiometry, searches for dark matter, or gravitational wave detection.

Introduction

Quantum sensing relies on the manipulation of internal or external degrees of freedom in atoms, molecules, opto-mechanical devices, photonic or solid-state systems, and covers various applications such as magnetometry (1–3), the definition of frequency standards (4, 5), short-range force measurements (6) or electromagnetic measurements (7, 8). Inertial sensors based on the coherent manipulation of superpositions of momentum states in atom interferometers have been developed for more than 25 years (9–11), with the goal to address various applications. Examples of remarkable achievements are tests of fundamental physics (12–16), metrology (17), or absolute gravimetry (18–21). Such precision measurements of gravito-inertial effects directly take benefit from the inherent accuracy and long-term stability of cold-atom sensors. These two properties can eventually be combined with the high-bandwidth of relative sensors, which is at the basis of sensor fusion (22). This approach is reminiscent of atomic clocks, where probing the stable atomic energy structure is used for stabilizing a microwave or optical oscillator (4, 5), or for tests of fundamental physics.

The extension of the applications of cold-atom inertial sensors to the measurement of time-varying signals has been confronted to their reduced sampling rate, which originates from their sequential operation and from the long interrogation time of the atoms that is required to achieve high inertial sensitivity. This limitation is, for example, an obstacle for applications to inertial navigation (23) or to fundamental research related to dark matter detection (24) or gravitational wave astronomy (25, 26). In this work, we report on the interleaved operation of a cold-atom inertial sensor, which operates with a sampling frequency of 3.75 Hz and features a high inertial sensitivity, as given by the 801 ms interrogation time of the atoms in the interferometer. The method

of interleaving, which we demonstrate for both static and dynamic rotation rate measurements, can be generalized to other atom interferometer architectures, and therefore paves the way to the development of high-bandwidth and high-sensitivity cold-atom inertial sensors.

Besides an increase in sensor bandwidth, we show that interleaving allows to efficiently average vibration noise (as $1/\tau$, with τ the integration time), which represents the most important noise source in cold-atom inertial sensors. As a consequence, we demonstrate a record rotation rate sensitivity of $3 \times 10^{-8} \text{ rad.s}^{-1}.\text{Hz}^{-1/2}$. Such a high sensitivity level allows us to characterize the systematic effects of a cold-atom gyroscope in a so-far unexplored range (27,28), and to stabilize them at the few $10^{-10} \text{ rad.s}^{-1}$ level. Previous works on atomic beam gyroscopes already demonstrated excellent sensitivities (29) and long term stabilities close to the state-of-the-art of optical gyroscopes (30). As the long-term instability of gyroscopes is a limiting factor in inertial navigation systems, achieving the performance of the best fiber-optics gyroscopes (31) was a long-standing goal, which we attain for the first time with a cold-atom sensor.

Results

Experimental setup

Experimental sequence and principle of the gyroscope. The core of the experimental setup used in this work has been described in (32), and is sketched in Fig. 1. The essential techniques are given in the Materials and Methods section, with further details in the Supplementary Materials. In short, we laser-cool Cesium atoms to a temperature of $1.2 \mu\text{K}$ and launch them vertically at a velocity of 5.0 m.s^{-1} . After a selection step of the $m_F = 0$ magnetic sublevel, we interrogate the atoms in the interferometer, and finally detect their state at the output of the interferometer, on their way down, using fluo-

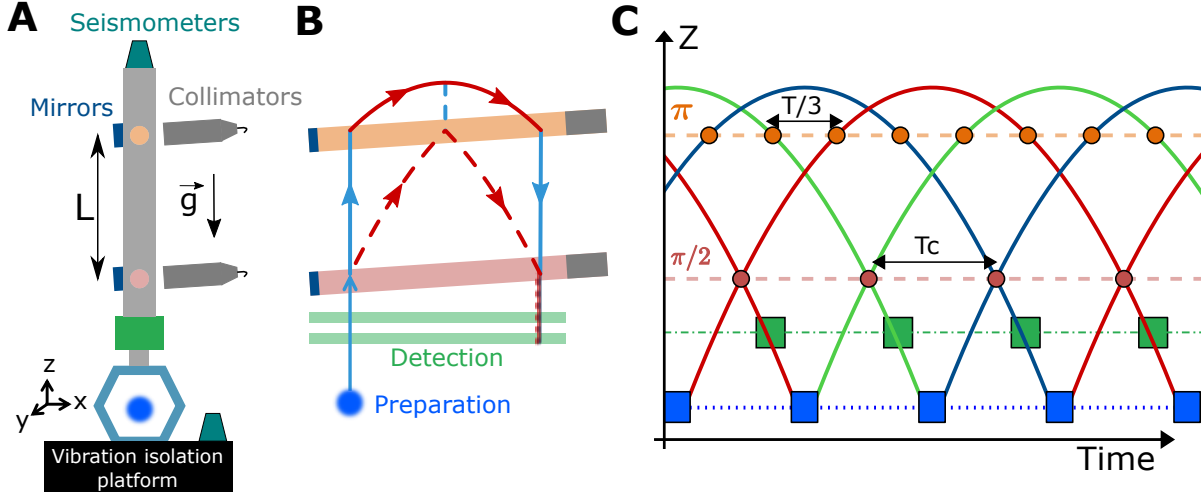


Figure 1: **Principle of the experiment.** **A:** sketch of the experiment, where the atoms are laser cooled (blue cloud) and launched vertically, interrogated by two Raman beams (brought from the gray collimators and retro-reflected on the blue mirrors), and detected on their way down (green box). The distance between the Raman beams is $L = \frac{3}{8}gT^2 \simeq 59$ cm. **B:** diagram of the atom interferometer in the (xz) plane (not to scale), with the blue and red lines respectively labeling the $|\vec{0}\rangle$ and $\hbar\vec{k}_{\text{eff}}$ momentum states. The dashed and plain lines show the two paths of the matter-waves in the interferometer, which enclose an area of 11 cm 2 . **C:** trajectories of the successively launched atom clouds in interleaved operation. Each interferometer has an interrogation time $2T = 801$ ms and the cycle time is $T_c = 2T/3 = 267$ ms. The $\pi/2$ pulses are shared between the atom clouds entering and exiting the interferometer.

rescence detection. We realize the light-pulse atom interferometer using two-photon stimulated Raman transitions with counter-propagating laser beams which couple the $|F = 3, m_F = 0\rangle$ and $|F = 4, m_F = 0\rangle$ clock states of the Cesium atom.

According to the Sagnac effect, the rotation sensitivity is proportional to the area between the 2 arms of the interferometer. Our gyroscope is based on a fountain configuration with 4 light pulses to create a folded geometry thanks to gravity (33). The symmetric 4 pulse fountain configuration allows to achieve a large area (11 cm 2 in this work) and leads to a vanishing sensitivity to constant linear accelerations. The interferometer phase shift, Φ , can be calculated from the relative phase between the two

Raman lasers, $\Delta\varphi_{\text{laser}}(t) = \vec{k}_{\text{eff}} \cdot \vec{r}_{b,t}(t) + \Delta\varphi(t)$, which is imprinted on the diffracted part of the matter-wave at the time t of the pulse. It reads:

$$\Phi = \vec{k}_{\text{eff}} \cdot \left[\vec{r}_b(0) - 2\vec{r}_t\left(\frac{T}{2}\right) + 2\vec{r}_t\left(\frac{3T}{2}\right) - \vec{r}_b(2T) \right] + \Delta\Phi^0, \quad (1)$$

where \vec{k}_{eff} is the two-photon wavevector, $\vec{r}_{b,t}(t)$ is the position of the mirror retro-reflecting the Raman lasers with respect to the center-of-mass of the free falling atoms (subscripts $\{b, t\}$ for bottom and top mirror, see Fig. 1), and $2T$ is the total interrogation time. The last term $\Delta\Phi^0$ is a controllable laser phase shift independent of inertial effects. The phase shift associated to the stationary Earth rotation rate $\vec{\Omega}_E$ is given by

$$\Phi_\Omega = \frac{1}{2} \vec{k}_{\text{eff}} \cdot \left(\vec{g} \times \vec{\Omega}_E \right) T^3, \quad (2)$$

where \vec{g} is the acceleration of gravity (34).

Interleaved operation. We employ a sequence of joint interrogation of successive interferometers, which is obtained by using the same $\pi/2$ Raman pulse for the atom clouds entering and exiting the interferometer zone (32). Consequently, the sensor can operate without dead times. The interleaved operation, which is reminiscent from the atom juggling technique of Ref. (35), is then implemented by extending this joint sequence to a multiple-joint sequence, as proposed in (36). The sequence of Raman pulses is given in Fig. 1. If we denote $2T = 801$ ms the total duration of the interferometer, we launch an atom cloud every $T_c = 2T/3 = 267$ ms, which supposes that a cloud is laser-cooled while 3 previously launched clouds are interrogated in the interferometer. Due to timing constraints, the loading time of the magneto-optical trap (MOT) is limited. The atoms are loaded in the MOT during 55 ms, and we detect 2×10^5 atoms at the end of the interferometer. The light scattered from the MOT atoms causes incoherent photon absorption and emission from the interrogated atoms and therefore a loss of contrast (36). The contrast of the interferometer is 7.4%, limited by the expansion of

the cloud during the free fall in the Raman beams of gaussian profile, and by the light scattered from the MOT.

Technical upgrades. We implemented several key upgrades of our setup compared to Ref. (32). First, we improved the detection noise which was limiting the sensitivity in (32). The equivalent one-shot phase noise is now 71 mrad, corresponding to a rotation noise of $8 \text{ nrad}\cdot\text{s}^{-1}\cdot\text{Hz}^{-1/2}$. Second, we implemented a real-time compensation of linear acceleration noise (22), and a servo-loop to operate the interferometer at mid-fringe, i.e. in its linear range. These techniques are described in the Materials and Methods section. These upgrades result in a sensor which effectively operates without dead times, as statistically very few points sit on the top or bottom of a fringe, where the sensitivity vanishes.

Rotation rate acquisition. Fig. 2 shows a 32.5 hours acquisition of rotation rate measurements obtained between September 23rd and 25th, 2017. To obtain this series of data, we alternated the direction of the Raman wavevector ($\pm\vec{k}_{\text{eff}}$) and computed the half-difference of two successive measurements to reject non-inertial (\vec{k}_{eff} -independent) effects, such as AC Stark shifts (see Methods and Supplementary Materials- section S1 for the details of the sequence, and section S2 for the raw data). In the following, we will analyze the sensitivity and the stability of the gyroscope from this acquisition.

Efficient averaging of vibration noise and record sensitivity

Vibration noise is the most important source of sensitivity degradation in cold-atom inertial sensors of large area (i.e. using long interrogation time and/or large momentum transfer techniques (37)). Efficient vibration isolation at low frequencies (below few Hz) is technically challenging (e.g. (38)) and not suited for field applications. We will show that interleaving allows to reduce the impact of this key noise source.

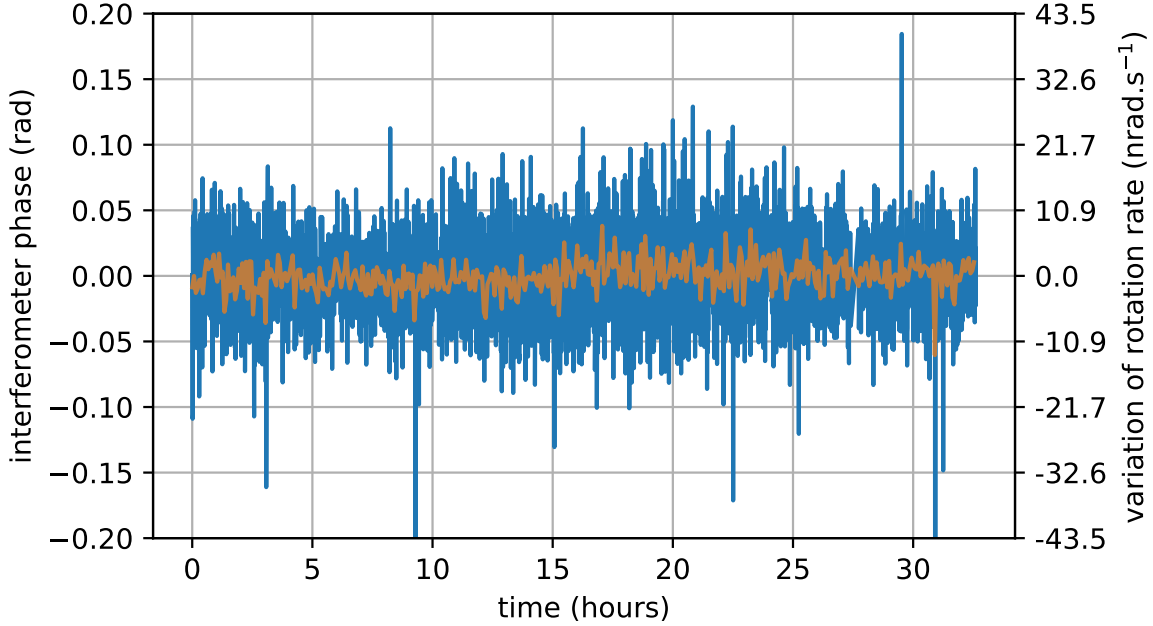


Figure 2: **Rotation rate measurement during 32.5 hours.** In the blue (orange) trace, each data point is the average over segments of 26.7 s (267 s) of raw inertial phase measurements. The right axis translates inertial phase to rotation rate using the scale factor of the gyroscope to stationary Earth rotation (from Eq. (2)).

In our sensor, the impact of inertial noise can be analyzed by considering a center of rotation located at the top Raman beam: inertial noise then appears as linear acceleration noise of both mirrors, plus rotation noise of the bottom mirror. The rotation noise translates into random variations of the angle $\theta_B(t)$ of the Raman beam with respect to a geostationary reference frame (34), and impacts the interferometer phase as $[\theta_B(2T) - \theta_B(0)]$ (Eq. (1)). In joint measurements, in which $\pi/2$ pulses are shared (occurring at times 0 and $2T$), the contribution of rotation noise cancels out when averaging N successive measurements (see Material and Methods for a derivation). Therefore, the gyroscope sensitivity should improve as τ^{-1} , where $\tau = 2NT$ is the integration time, instead of $\tau^{-1/2}$ in the case of uncorrelated measurements impacted by rotation

noise.

Besides averaging rotation noise, the interleaved operation of our sensor allows us to reduce the impact of residual linear acceleration noise: because our sampling frequency ($1/T_c = 3.75$ Hz) is higher than the frequencies at which the acceleration noise mostly contributes (around 0.5 Hz, see Table S1 in Supplementary Materials), correlations appear between successive measurements, yielding a scaling of the sensitivity that approaches τ^{-1} (rather than $\tau^{-1/2}$).

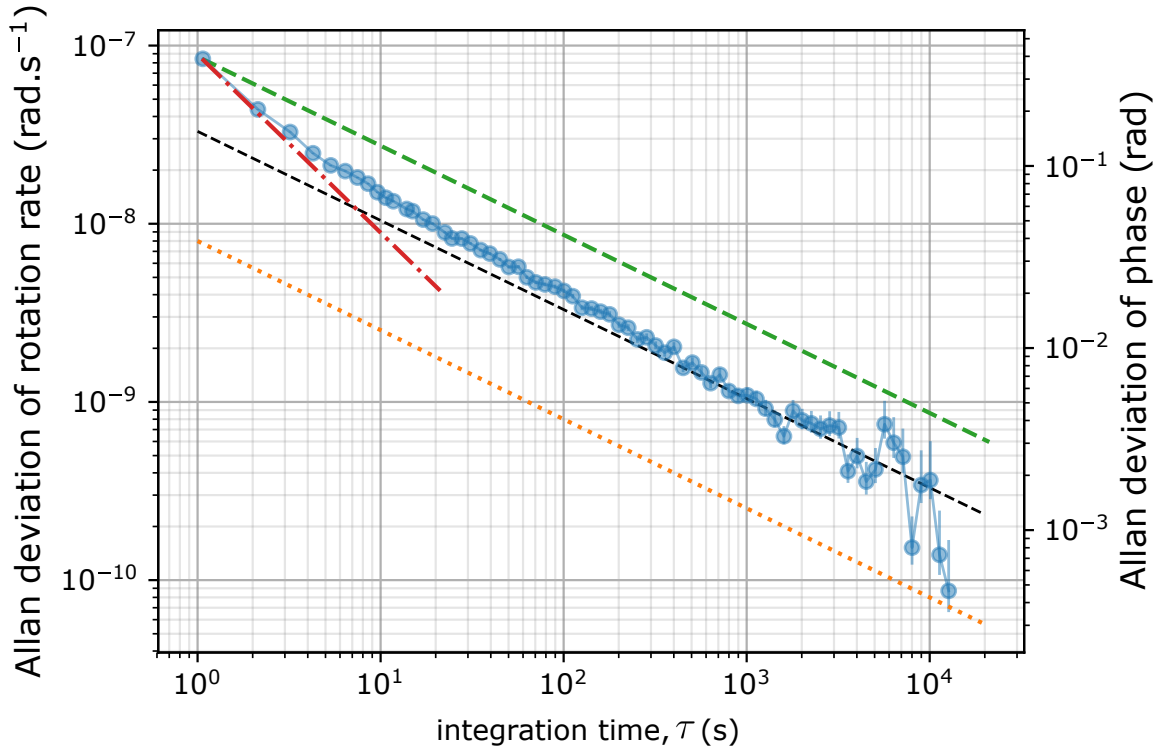


Figure 3: **Gyroscope sensitivity.** Stability analysis of a 11.3 hour portion of the rotation rate measurements of Fig. 2, between 1:22 and 12:47 on September 24th, 2017. The error bars represent the 68 % confidence intervals on the estimation of the Allan deviation. Dashed black line: $3.3 \times 10^{-8} \text{ rad.s}^{-1} \times \tau^{-1/2}$. Green dashed line: $\tau^{-1/2}$ scaling from the one shot Allan deviation. Red dotted-dashed line: τ^{-1} scaling from the one shot Allan deviation. Orange dotted line: detection noise limit corresponding to $8 \times 10^{-9} \text{ rad.s}^{-1} \times \tau^{-1/2}$.

Fig. 3 shows the Allan deviation of the gyroscope stability for a 11.3 hour portion of night data of Fig. 2. The improvement of the sensitivity as τ^{-1} for integration times up to $\simeq 7$ s is clear. The stability then gradually enters the $\tau^{-1/2}$ regime characteristic of uncorrelated white noise, corresponding to a sensitivity of 3×10^{-8} rad.s⁻¹.Hz^{-1/2}. This sensitivity, which improves by more than a factor of 3 on our previous result (32), establishes the new record for cold atom gyroscopes. As a comparison, our short term sensitivity competes favorably with that of the best fiber-optics gyroscopes (31). Such sensitivity enables to study several systematic effects affecting a cold atom gyroscope, for the first time in the range of low 10^{-9} rad.s⁻¹.

Systematic effects and gyroscope long term stability

A systematic shift specific to the interleaved interrogation originates from the light scattered from the MOT towards the atoms interrogated in the interferometer (36). The MOT scattered light is close to resonance and induces a loss of contrast and a differential light shift (AC Stark shift). The influence of induced light shifts is reduced by the spin-echo-like four-pulse sequence, and by the use of \vec{k}_{eff} reversal: alternating $\pm \hbar \vec{k}_{\text{eff}}$ momentum transfers changes the sign of the inertial phase shift but not the one of the clock-terms (e.g. differential light shift), which are rejected when taking the half-difference of two measurements (as done in Fig. 2). We measured the residual effect, and showed that it corresponds to an instability below 7×10^{-11} rad.s⁻¹ (see Supplementary Materials). Although currently negligible, this effect is purely technical, and could be resolved by having the MOT and the detection region out of view from the atom interferometer region in future designs.

The most important systematic effects in atom interferometers with separated Raman beams originate from relative wavefront mismatch coupled to deviations of the

atom trajectories with respect to the ideal one (27,39). In our system, a relative angular misalignment $\vec{\delta\theta}$ between the top and bottom mirrors used to retro-reflect the Raman beams (Fig. 1), coupled with an error of launch velocity $\vec{\delta v}$ (with respect to a velocity of $-\vec{g}T$ at the first Raman pulse) in the (y, z) plane results in a phase shift

$$\Delta\Phi = 2Tk_{\text{eff}}(\delta v_y\delta\theta_y + \delta v_z\delta\theta_z) = 12 \text{ mrad} \times \left(\frac{\delta v_{y,z}}{1 \text{ mm}\cdot\text{s}^{-1}}\right) \times \left(\frac{\delta\theta_{y,z}}{1 \text{ }\mu\text{rad}}\right). \quad (3)$$

We explain in the Materials and Methods section how we set the parallelism between the two Raman beams and the velocity of the atoms to approach the ideal trajectory, in order to achieve an uncertainty on the residual systematic shift of 21 mrad (i.e. $4.6 \text{ nrad}\cdot\text{s}^{-1}$, from Eq. (2)).

After this systematic analysis and the corresponding fine-tuning of the apparatus, we recorded the rotation rate acquisition displayed on Fig. 2. The stability of the gyroscope over the entire acquisition is analyzed in the Supplementary Materials (Fig. S5), and is in agreement with that read from Fig. 3 for shorter integration times.

Dynamic rotation rate measurements.

We use the unprecedented sampling rate and inertial sensitivity of our gyroscope to perform measurements of weak dynamic rotation rates. To this end, we modulate the orientation of the experiment around the y axis. This was performed by applying a force on the bottom plate linking the experimental frame to the vibration isolation platform, via the voice-coil actuator controlling the tilt θ_x of the apparatus. We apply sinusoidal modulations of the form $\theta_x(t) = \theta_0 \sin(\omega t)$ with a period $2\pi/\omega$ and with an amplitude θ_0 of few 10^{-7} rad. The resulting rotation rate is of the form $\vec{\Omega}(t) = \Omega_0 \cos(\omega t)\hat{u}_y$, with $\Omega_0 = \omega\theta_0$. The measurements are reported in Fig. 4 for modulation periods of 5 s and 10 s. The respective modulation amplitudes are 2.3×10^{-7} rad and 3.4×10^{-7} rad. Panels A and B show the atomic phase extracted from the transition probability, $P(t)$,

which follows the sinusoidal modulation. The total rotation signal from the atom interferometer is the sum of this atomic phase and the phase compensated in real time. A Fourier analysis of the total signal is shown in panel C. Within our frequency resolution, we find that the amplitude of the reconstructed rotation rate signal agrees with the expectation of Ω_0 with a relative precision of 5%. A more detailed analysis is presented in the Supplementary Materials (section S5). Our proof-of-principle experiment, performed in a so-far unexplored range of time resolution and inertial sensitivity for a cold-atom sensor, demonstrates the impact of interleaved atom interferometry for dynamic measurements.

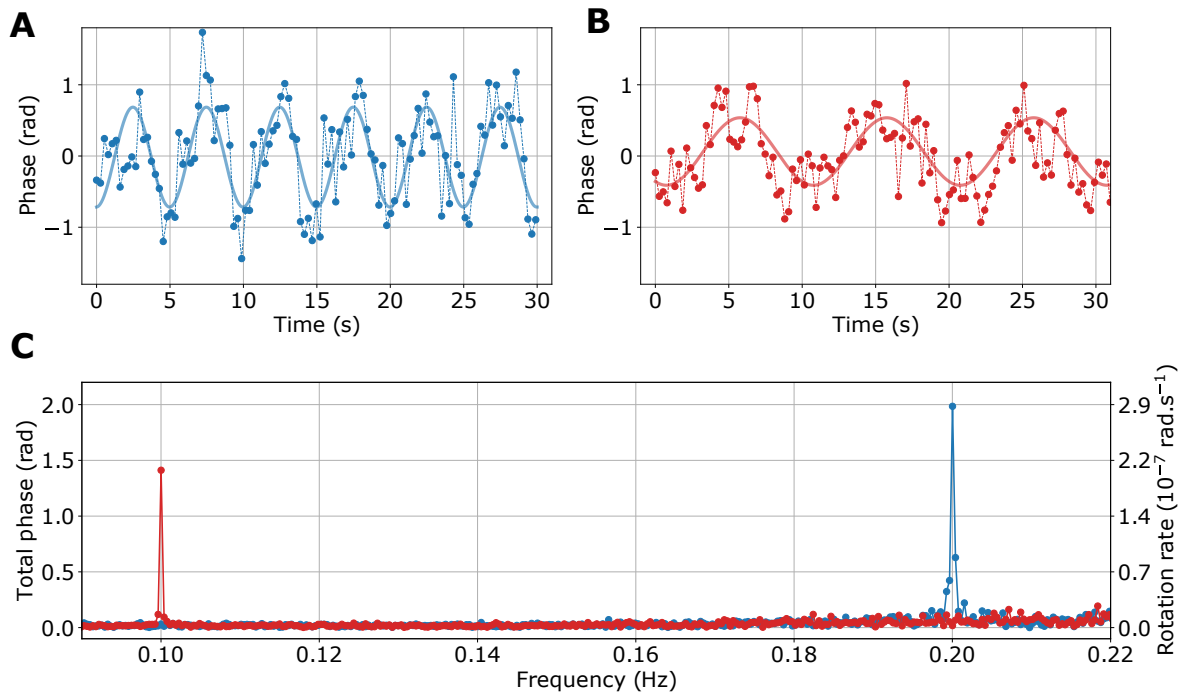


Figure 4: **Measurement of dynamic rotation rates.** Atom interferometer phase deduced from the transition probability, for rotation rate modulations of 5 s period (A) and 10 s period (B). Plain line: sinusoidal fit to guide the eye. C): Fourier analysis of the total rotation rate signal, with a frequency resolution is 0.37 mHz.

Discussion

We demonstrated the method of interleaving in a large-area atom interferometer, as a way to reach high sampling frequencies and high inertial sensitivities together. Interleaving enables to efficiently average vibration noise (the largest noise source in cold-atom inertial sensors), and is thus a promising way of reaching the quantum projection noise limit, a necessary condition before increasing the atom flux or implementing schemes to approach the Heisenberg limit. As a result, we demonstrated record short term sensitivities for a cold-atom gyroscope, and could thus characterize systematic effects in a so-far unexplored range. The rotation rate sensitivity and stability which we achieved competes with that of the best strategic-grade fiber-optics gyroscopes (long-term stability in the range of 5×10^{-10} rad.s⁻¹ (31)). Our results thus pave the way for a change of technology in future high-precision inertial navigation systems.

In our setup, the maximum number of interleaved measurements is technically limited to 3 because of the arrangement of our detection system with respect to the MOT region (see Materials and Methods). In a dedicated design, e.g. where the detection region would be out of view from the upcoming clouds, sampling frequencies of 20 Hz or higher could be reached. As an alternative, the use of atoms characterized by different transition wavelengths for the cooling/detection/atom interferometer would be beneficial, in order to circumvent the effects associated with the scattered light from the source or the detected atoms. Our technique is thus well-suited to ongoing developments of atom interferometers with alkaline-Earth atoms (40).

Interleaving ties well with laser-cooling techniques, which are able to rapidly (in less than 100 ms) produce cold samples with more than 10^7 atoms. Laser cooling beyond optical molasses such as degenerate Raman sideband cooling appear as a suitable

solution for an increased brightness without compromising the cycling frequency. Interleaving is, in principle, also compatible with the production of ultracold, collimated, atom sources (16), provided they can be produced (41) or extracted at sufficiently high (several Hz) repetition rates.

The method of interleaved atom interferometry can be applied to different sensor architectures, such as multi-axes accelerometers (by alternating measurements along different axes at a high repetition rate), gravimeters or gradiometers. For example, interleaving can be exploited to realize a gravimeter of both high accuracy and high sensitivity in a single instrument, potentially allowing to surpass superconducting gravimeters that currently feature record sensitivities but require regular calibrations. As such, interleaving is representative of the flexibility of cold atoms for realizing versatile inertial sensors, as compared to architectures involving macroscopic masses and electro-mechanical systems. Regarding fundamental physics applications, reaching high sampling rates is a prerequisite for future studies on dark-matter with atomic accelerometers (24), as well as for gravitational wave detection with atom interferometers (25,26). Interleaving is therefore a key concept for future applications of cold-atom inertial sensors.

Materials and Methods

Details of the experiment

Cesium atoms loaded from a 2D Magneto-Optical Trap (MOT) are trapped and laser-cooled in a 3D-MOT. We launch the atoms vertically at a velocity of $5.0 \text{ m}\cdot\text{s}^{-1}$ using moving molasses with a (3D) cloud temperature of $1.2 \mu\text{K}$. After the MOT and prior to the interrogation, the atoms are prepared in the $|F = 4, m_F = 0\rangle$ state using a selection scheme based on the Stern-Gerlach effect (magnetic deflection of the atoms in $m_F \neq 0$

states). Light pulse interferometry is realized using two phase-locked Raman lasers which couple the Cesium clock states (hyperfine splitting of 9.192 GHz). The Raman lasers have a wavelength close to the D_2 line (wavelength $\lambda \simeq 852$ nm) and are detuned by 470 MHz from the excited state to reduce incoherent scattering. The impact of residual relative Raman laser phase noise has been estimated to 50 mrad per shot of atom interferometer phase. The Raman lasers are sent to the atoms through two optical windows separated by $L = \frac{3}{8}gT^2 \simeq 59$ cm, with an interrogation time $2T = 801$ ms. We use gaussian Raman beams with $1/e^2$ diameter equal to 40 mm and about 120 mW of total power. The interferometer output signal is determined by the probability of transition, P , from the $F = 4$ to the $F = 3$ state, which is read out via fluorescence detection of the two levels' populations after the atom interferometer light-pulse sequence. The probability of transition is modulated according to $P = P_0 + A \sin \Phi$, where $C = 2A$ is the interferometer contrast and Φ the interferometer phase.

Our experiment uses retro-reflected Raman beams, such as to form two pairs of Raman beams inducing two transitions: one in the $+\vec{k}_{\text{eff}}$ direction, and another in the $-\vec{k}_{\text{eff}}$ direction. Selectivity of the $\pm\vec{k}_{\text{eff}}$ transitions is provided by tilting the Raman beams by an angle $\theta \simeq 3.80$ degrees with respect to the horizontal, in order to introduce a Doppler shift ($\pm k_{\text{eff}}gT \sin \theta/2\pi \simeq \pm 611$ kHz at the first and last $\pi/2$ pulses) which is much larger than the width of the atom Doppler distribution (~ 40 kHz). To follow the resonance condition at each Raman pulse, we step-wise change the relative frequency between the two Raman lasers during the sequence, such as to match the values given by the underlying frequency chirp pattern (see details in Fig. S2 of Supplementary Materials). To apply the frequency steps, we use a direct digital synthesizer (DDS) driven by an FPGA.

Real-time compensation of vibration noise and mid-fringe lock. We measure the vibra-

tions of the setup with two broadband seismometers (model *Trillium Compact 120 s* from *Nanometrics*) located at the bottom and top of the experimental frame (see Fig. 1). From the measured signal, we estimate the interferometer phase shift due to vibrations and apply a corresponding phase jump to the relative phase of the Raman lasers 15 ms before the last pulse. This allows us to reduce the standard deviation of the interferometer phase from about 3.2 rad to 0.5 rad. To work within the linear regime where the sensitivity is maximal, we alternate measurements on both sides of a fringe, and compute an error signal from two successive measurements of the transition probability. This error signal is integrated and used to servo-lock the interferometer at mid-fringe, via a feedback on the Raman laser relative phase. More details are given in the Supplementary Materials, section S1.

Efficient averaging of vibration noise

Following Eq. (1), and assuming that the Raman lasers are oriented purely in the x direction, the 4-light-pulse atom interferometer phase shift is given by (we neglect the duration of the Raman pulse):

$$\Phi = k_{\text{eff}} [x_b(0) - 2x_t(T/2) + 2x_t(3T/2) - x_b(2T)], \quad (4)$$

with $x_{b,t}(t)$ the position of the bottom and top retro-mirrors with respect to the free-falling atom cloud. The phase shift can be re-written as

$$\begin{aligned} \Phi &= k_{\text{eff}} [x_t(0) - 2x_t(T/2) + 2x_t(3T/2) - x_t(2T)] + k_{\text{eff}} \left([x_b(0) - x_t(0)] - [x_b(2T) - x_t(2T)] \right) \\ &= \Phi_t^{\text{acc}} + k_{\text{eff}} L (\theta_b(0) - \theta_b(2T)), \end{aligned} \quad (5)$$

with $L = \frac{3}{8}gT^2$ the distance between the bottom and top mirrors, and Φ_t^{acc} the term associated to the linear acceleration of the top mirror. The second term represents pure

rotation of the bottom mirror about the position of the top one. Recalling that $T_c = 2T/3$ and writing as $\Phi_i = \Phi(iT_c)$ the atom interferometer phase at cycle i , the mean phase after N measurement reads

$$\bar{\Phi}_N = \frac{1}{N} \sum_{i=0}^{N-1} \Phi_i = \frac{1}{N} \sum_{i=0}^{N-1} \left(k_{\text{eff}} L [\theta_b(iT_c) - \theta_b((i+3)T_c)] + \delta\tilde{\phi}_i \right). \quad (6)$$

The term $\delta\tilde{\phi}_i$ encompasses contributions of detection noise, uncompensated linear acceleration noise and laser phase noise. When expanding the sum in Eq. (6), most of the θ_b terms mutually cancel, such that the mean phase reads

$$\bar{\Phi}_N = k_{\text{eff}} L \frac{\theta_b(0) - \theta_b((N+2)T_c)}{N} + \frac{1}{N} \sum_{i=0}^{N-1} \delta\tilde{\phi}_i. \quad (7)$$

This equation shows that the random rotation noise averages as N^{-1} (first term). The second term represents the uncorrelated noise contributions of standard deviation $\sigma_{\delta\phi}$. Their sum equals $\sqrt{N} \times \sigma_{\delta\phi}$, which corresponds to a scaling of the phase sensitivity as $N^{-1/2}$.

Besides rotation noise, uncompensated linear accelerations in the frequency range [0.1 – 1] Hz contribute to a large part the interferometer phase noise (see the Supplementary Materials section S3 for details). This contribution, estimated to typically about 500 mrad per shot, dominates the noise budget and may prevent from observing a clear τ^{-1} scaling of the gyroscope sensitivity. Interleaving, however, allows to over-sample these fluctuations, thus introducing correlations between successive measurements, which also contributes to the τ^{-1} dependence of the instrument sensitivity.

Alignment of the two Raman beams and atom trajectory

We set the parallelism between the top and bottom Raman beams by means of a two-axis piezo-motorized mirror mount with 0.7 μrad resolution. By optimizing the contrast of the interferometer, we approach the parallelism with an uncertainty of about

3 μrad , which is required for the matter-waves to recombine at the output of the interferometer. For the fine adjustment, we measure the dependence of the phase shift of Eq. (3), $\Delta\Phi = 2Tk_{\text{eff}}(\delta v_y \delta\theta_y + \delta v_z \delta\theta_z)$, on $\delta\theta_{y,z}$ and $\delta v_{y,z}$ (as defined in the main text). To this end, we set the atom trajectory in the (y, z) directions by varying the tilt of the experiment (y direction) and the launch velocity during the moving molasses phase (z direction). In the z direction, we could zero the systematic effect with an uncertainty of 5 mrad. This amounts to set the velocity of the atoms at the first Raman pulse to the ideal velocity ($v_z = gT$) with an uncertainty of 0.6 $\text{mm}\cdot\text{s}^{-1}$, and to set the parallelism between two mirrors in the z direction with an uncertainty of 0.7 μrad .

The minimization of the systematic shift in the y direction was technically more difficult to achieve than in the z direction: recording the dependence of the phase shift on $\delta\theta_y$ for various velocities required to tilt the entire apparatus by several mrad in order to vary δv_y by several $\text{mm}\cdot\text{s}^{-1}$. This procedure required to manually move masses on the base plate of the experiment sitting on a floating vibration isolation platform, which introduced instabilities. We managed to set the y -velocity close to the ideal velocity ($v_y = 0$) with an uncertainty of 1.8 $\text{mm}\cdot\text{s}^{-1}$. The residual shift corresponds to a phase variation of 21 mrad per μrad of $\delta\theta_y$ variation.

Limitation to the number of interleaved interferometers

When trying 5 interleaved cycles, we observed a dramatic loss of contrast of the interferometer. The reason is that when a (descending) atom cloud at the output of the interferometer enters the detection region, a part of the light scattered by the atoms is directed towards the (ascending) cloud, which optically pumps atoms to unwanted magnetic states and heats them before they enter the interferometer.

Supplementary Materials

Supplementary material for this article is available and contains:

Supplementary text, Sections S1 to S6

Figures S1 to S5

Table S1

References (22, 34, 42)

References

1. D. Sheng, S. Li, N. Dural, M. V. Romalis, Subfemtotesla scalar atomic magnetometry using multipass cells. *Phys. Rev. Lett.* **110**, 160802 (2013).
2. I. Gross, W. Akhtar, V. Garcia, L. J. Martinez, S. Chouaieb, K. Garcia, C. Carrtro, A. Barthlmy, P. Appel, P. Maletinsky, J.-V. Kim, J. Y. Chauleau, N. Jaouen, M. Viret, M. Bibes, S. Fusil, V. Jacques, Real-space imaging of non-collinear antiferromagnetic order with a single-spin magnetometer. *Nature* **549**, 252 (2017).
3. R. Jiménez-Martínez, J. Kołodyński, C. Troullinou, V. G. Lucivero, J. Kong, M. W. Mitchell, Signal tracking beyond the time resolution of an atomic sensor by kalman filtering. *Phys. Rev. Lett.* **120**, 040503 (2018).
4. M. Takamoto, F.-L. Hong, R. Higashi, H. Katori, An optical lattice clock. *Nature* **435**, 321 (2005).
5. R. Le Targat, L. Lorini, Y. Le Coq, M. Zawada, J. Guna, M. Abgrall, M. Gurov, P. Rosenbusch, D. G. Rovera, B. Nagrny, R. Gartman, P. G. Westergaard, M. E. Tobar, M. Lours, G. Santarelli, A. Clairon, S. Bize, P. Laurent, P. Lemonde,

- J. Lodewyck, Experimental realization of an optical second with strontium lattice clocks. *Nature Communications* **4**, 2109 (2013).
6. M. G. Tarallo, T. Mazzoni, N. Poli, D. V. Sutyryn, X. Zhang, G. M. Tino, Test of einstein equivalence principle for 0-spin and half-integer-spin atoms: Search for spin-gravity coupling effects. *Phys. Rev. Lett.* **113**, 023005 (2014).
 7. T. Bagci, A. Simonsen, S. Schmid, L. G. Villanueva, E. Zeuthen, J. Appel, J. M. Taylor, A. Sørensen, K. Usami, A. Schliesser, E. S. Polzik, Optical detection of radio waves through a nanomechanical transducer. *Nature* **507**, 81 (2014).
 8. A. Facon, E.-K. Dietsche, D. Grosso, S. Haroche, J.-M. Raimond, M. Brune, S. Gleyzes, A sensitive electrometer based on a rydberg atom in a schrödinger-cat state. *Nature* **535**, 262 (2016).
 9. C. Bordé, Atomic interferometry with internal state labelling. *Physics Letters A* **140**, 10–12 (1989).
 10. M. Kasevich, S. Chu, Atomic interferometry using stimulated raman transitions. *Phys. Rev. Lett.* **67**, 181–184 (1991).
 11. F. Riehle, T. Kisters, A. Witte, J. Helmcke, C. J. Bordé, Optical ramsey spectroscopy in a rotating frame: Sagnac effect in a matter-wave interferometer. *Phys. Rev. Lett.* **67**, 177–180 (1991).
 12. R. Bouchendira, P. Cladé, S. Guellati-Khlifa, F. Nez, F. Biraben, New Determination of the Fine Structure Constant and Test of the Quantum Electrodynamics. *Physical Review Letters* **106** (2011).

13. S. Lepoutre, A. Gauguet, G. Tréneç, M. Büchner, J. Vigué, He-mckellar-wilkens topological phase in atom interferometry. *Phys. Rev. Lett.* **109**, 120404 (2012).
14. L. Zhou, S. Long, B. Tang, X. Chen, F. Gao, W. Peng, W. Duan, J. Zhong, Z. Xiong, J. Wang, Y. Zhang, M. Zhan, Test of Equivalence Principle at 10^{-8} Level by a Dual-Species Double-Diffraction Raman Atom Interferometer. *Physical Review Letters* **115** (2015).
15. M. Jaffe, P. Haslinger, V. Xu, P. Hamilton, A. Upadhye, B. Elder, J. Khoury, H. Mller, Testing sub-gravitational forces on atoms from a miniature in-vacuum source mass. *Nature Physics* **13**, 938–942 (2017).
16. P. Asenbaum, C. Overstreet, T. Kovachy, D. D. Brown, J. M. Hogan, M. A. Kasevich, Phase Shift in an Atom Interferometer due to Spacetime Curvature across its Wave Function. *Physical Review Letters* **118** (2017).
17. G. Rosi, F. Sorrentino, L. Cacciapuoti, M. Prevedelli, G. M. Tino, Precision measurement of the Newtonian gravitational constant using cold atoms. *Nature* **510**, 518–521 (2014).
18. A. Peters, K. Y. Chung, S. Chu, High-precision gravity measurements using atom interferometry. *Metrologia* **38**, 25 (2001).
19. C. Freier, M. Hauth, V. Schkolnik, B. Leykauf, M. Schilling, H. Wziontek, H.-G. Scherneck, J. Müller, A. Peters, Mobile quantum gravity sensor with unprecedented stability. *J. Phys. Conf. Ser.* **723**, 012050 (2016).
20. Y. Bidel, N. Zahzam, C. Blanchard, A. Bonnin, M. Cadoret, A. Bresson, D. Rouxel, M. F. Lequentrec-Lalancette, Absolute marine gravimetry with matter-wave interferometry. *Nature Communications* **9**, 627 (2018).

21. R. Karcher, A. Imanaliev, S. Merlet, F. Pereira dos Santos, Improving the accuracy of atom interferometers with ultracold sources. *ArXiv e-prints* (2018).
22. J. Lautier, L. Volodimer, T. Hardin, S. Merlet, M. Lours, F. Pereira Dos Santos, A. Landragin, Hybridizing matter-wave and classical accelerometers. *Applied Physics Letters* **105**, 144102 (2014).
23. C. Jekeli, Navigation Error Analysis of Atom Interferometer Inertial Sensor. *Navigation* **52**, 1–14 (2005).
24. P. W. Graham, D. E. Kaplan, J. Mardon, S. Rajendran, W. A. Terrano, Dark matter direct detection with accelerometers. *Phys. Rev. D* **93**, 075029 (2016).
25. W. Chaibi, R. Geiger, B. Canuel, A. Bertoldi, A. Landragin, P. Bouyer, Low frequency gravitational wave detection with ground-based atom interferometer arrays. *Physical Review D* **93** (2016).
26. P. W. Graham, J. M. Hogan, M. A. Kasevich, S. Rajendran, Resonant mode for gravitational wave detectors based on atom interferometry. *Phys. Rev. D* **94**, 104022 (2016).
27. A. Gauguier, B. Canuel, T. Lévèque, W. Chaibi, A. Landragin, Characterization and limits of a cold-atom sagnac interferometer. *Phys. Rev. A* **80**, 063604 (2009).
28. P. Berg, S. Abend, G. Tackmann, C. Schubert, E. Giese, W. Schleich, F. Narducci, W. Ertmer, E. Rasel, Composite-Light-Pulse Technique for High-Precision Atom Interferometry. *Physical Review Letters* **114** (2015).
29. T. L. Gustavson, A. Landragin, M. A. Kasevich, Rotation sensing with a dual atom-interferometer sagnac gyroscope. *Classical and Quantum Gravity* **17**, 2385 (2000).

30. D. S. Durfee, Y. K. Shaham, M. A. Kasevich, Long-Term Stability of an Area-Reversible Atom-Interferometer Sagnac Gyroscope. *Physical Review Letters* **97** (2006).
31. H. C. Lefèvre, The fiber-optic gyroscope, a century after Sagnac's experiment: The ultimate rotation-sensing technology? *Comptes Rendus Physique* **15**, 851–858 (2014). ; For recent performances, see, e.g. iXblue ultimate-performance Fiber-Optic Gyroscope (FOG).
32. I. Dutta, D. Savoie, B. Fang, B. Venon, C. Garrido Alzar, R. Geiger, A. Landragin, Continuous Cold-Atom Inertial Sensor with 1 nrad / sec Rotation Stability. *Physical Review Letters* **116** (2016).
33. B. Canuel, F. Leduc, D. Holleville, A. Gauguier, J. Fils, A. Viridis, A. Clairon, N. Dimarcq, C. J. Bordé, A. Landragin, P. Bouyer, Six-axis inertial sensor using cold-atom interferometry. *Phys. Rev. Lett.* **97**, 010402 (2006).
34. J. K. Stockton, K. Takase, M. A. Kasevich, Absolute Geodetic Rotation Measurement Using Atom Interferometry. *Physical Review Letters* **107** (2011).
35. R. Legere, K. Gibble, Quantum scattering in a juggling atomic fountain. *Phys. Rev. Lett.* **81**, 5780–5783 (1998).
36. M. Meunier, I. Dutta, R. Geiger, C. Guerlin, C. L. Garrido Alzar, A. Landragin, Stability enhancement by joint phase measurements in a single cold atomic fountain. *Physical Review A* **90** (2014).
37. S. M. Dickerson, J. M. Hogan, A. Sugarbaker, D. M. S. Johnson, M. A. Kasevich, Multiaxis Inertial Sensing with Long-Time Point Source Atom Interferometry. *Physical Review Letters* **111** (2013).

38. J. M. Hensley, A. Peters, S. Chu, Active low frequency vertical vibration isolation. *Review of Scientific Instruments* **70**, 2735–2741 (1999).
39. G. Tackmann, P. Berg, C. Schubert, S. Abend, M. Gilowski, W. Ertmer, E. M. Rasel, Self-alignment of a compact large-area atomic sagnac interferometer. *New Journal of Physics* **14**, 015002 (2012).
40. L. Hu, N. Poli, L. Salvi, G. M. Tino, Atom interferometry with the sr optical clock transition. *Phys. Rev. Lett.* **119**, 263601 (2017).
41. J. Rudolph, W. Herr, C. Grzeschik, T. Sterneke, A. Grote, M. Popp, D. Becker, H. Mntinga, H. Ahlers, A. Peters, C. Lmmerzähl, K. Sengstock, N. Gaaloul, W. Ertmer, E. M. Rasel, A high-flux bec source for mobile atom interferometers. *New Journal of Physics* **17**, 065001 (2015).
42. P. Cheinet, B. Canuel, F. P. D. Santos, A. Gauguier, F. Yver-Leduc, A. Landragin, Measurement of the sensitivity function in a time-domain atomic interferometer. *IEEE Transactions on Instrumentation and Measurement* **57**, 1141–1148 (2008).

Acknowledgments

We thank F. Pereira Dos Santos for a careful reading of the manuscript.

Funding: We acknowledge the financial support from Ville de Paris (project HSENS-MWGRAV), FIRST-TF (ANR-10-LABX-48-01), Centre National d’Etudes Saptiales (CNES), Sorbonne Universités (project SU-16-R-EMR-30, LORINVACC) and Action Spécifique du CNRS Gravitation, Références, Astronomie et Métrologie (GRAM). B.F. was funded by Conseil Scientifique de l’Observatoire de Paris, D.S. by Direction Générale de l’Armement, and M.A. by the EDPIF doctoral school.

Author contributions: D.S., M.A., B.F. performed the experiments and L.A.S. contributed to the dynamic rotation rate measurements. D.S., R.G. and M.A. analyzed the data. R.G. and D.S. wrote the manuscript. A.L. conceived the experiment. R.G. and A.L. supervised the research. All authors discussed the manuscript.

Competing Interests: The authors declare that they have no competing interests.

Data and materials availability: All data needed to evaluate the conclusions in the paper are present in the paper and the Supplementary Materials. Additional data available from authors upon request.

Supplementary Materials

Section S1: Real-time compensation of vibration noise, mid-fringe lock, and details of the sequence

We calculate in real time the linear acceleration phase of the atom interferometer and compensate for it by applying a phase jump Φ_{RTC} at each cycle in the phase lock loop (PLL) of the Raman lasers (22). Specifically, we record, for each interferometer cycle, the signals of two seismometers during 786 ms, and compute the vibration phase shift by applying the sensitivity function of the 4 pulse interferometer to the half sum of the seismometer signals. As the transfer of the phase jump information to the direct digital synthesizer driving the PLL takes about 10 ms, we stop the seismometer acquisition 15 ms before the end of the cycle (yielding $801 - 15 = 786$ ms). This corresponds to an (estimated) 60 mrad rms error in the evaluation of the vibration phase.

Fig. 5 shows the histogram (in blue) of the estimated vibration phase, corresponding to a phase noise of 3.2 rad in standard deviation. The real time compensation of vibration allows to work within the linear response of the interferometer by reducing the phase spread to 0.52 rad, i.e. by a factor of 6 (orange histogram).

To work around mid-fringe on long-term acquisitions, an extra phase jump $\Phi_{\text{SRS},i} = \Phi_{\text{MFL},i} + (-1)^i \times \frac{\pi}{2}$ is added to $\Phi_{\text{RTC},i}$ at each cycle i . The value of the mid-fringe lock (MFL) phase is servoed by alternating measurements on both sides of a fringe with the application of successive $\pm\pi/2$ phase shifts (see Fig. 6, top panel). At the i^{th} cycle, the error signal of the loop is calculated as

$$\epsilon_i = (-1)^i (P_i - P_{i-1}), \quad (8)$$

where P_i is the transition probability at the i^{th} cycle. The correction is a pure integrator,

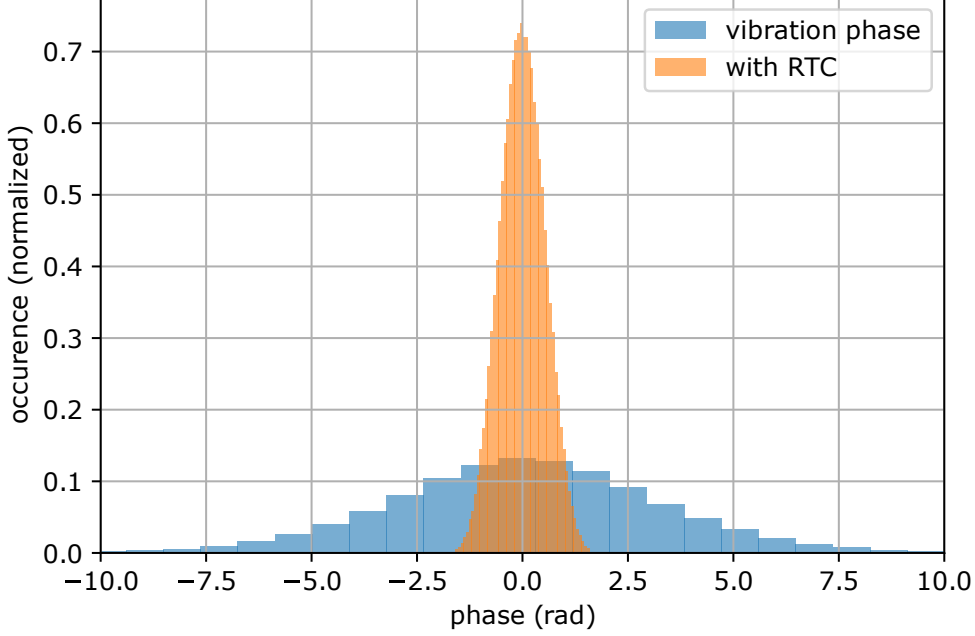


Figure 5: Histogram of the vibration phase and of the interferometer phase with real time compensation (RTC) of vibration. The standard deviation of the vibration phase (interferometer phase) is 3.2 (0.52) rad.

with the value of the phase at cycle i given by:

$$\Phi_{\text{MFL},i} = G \sum_{p=0}^i \epsilon_p \quad (9)$$

where G is the gain of the lock. The value $\Phi_{\text{MFL},i}$ is calculated at cycle i and applied at cycle $i + 1$. Once the lock has converged (typically after 50 s for a gain $G = 30$), the value of the interferometer phase can be directly read from Φ_{MFL} . The total phase of the atom interferometer (for each value of \vec{k}_{eff}) is computed as follows:

$$\Phi_i = (-1)^i \frac{P_i - P_{i-1}}{2A} + \frac{1}{2} (\Phi_{\text{SRS},i} + \Phi_{\text{SRS},i-1}), \quad (10)$$

where A is the fringe amplitude. The stability of the interferometer phase (as analyzed in Fig. 3 of the main text) is mainly given by the first term of Eq. (10) at short term

(for integration times below the mid-fringe locking point), while the second term is representative of the phase stability once the lock has converged.

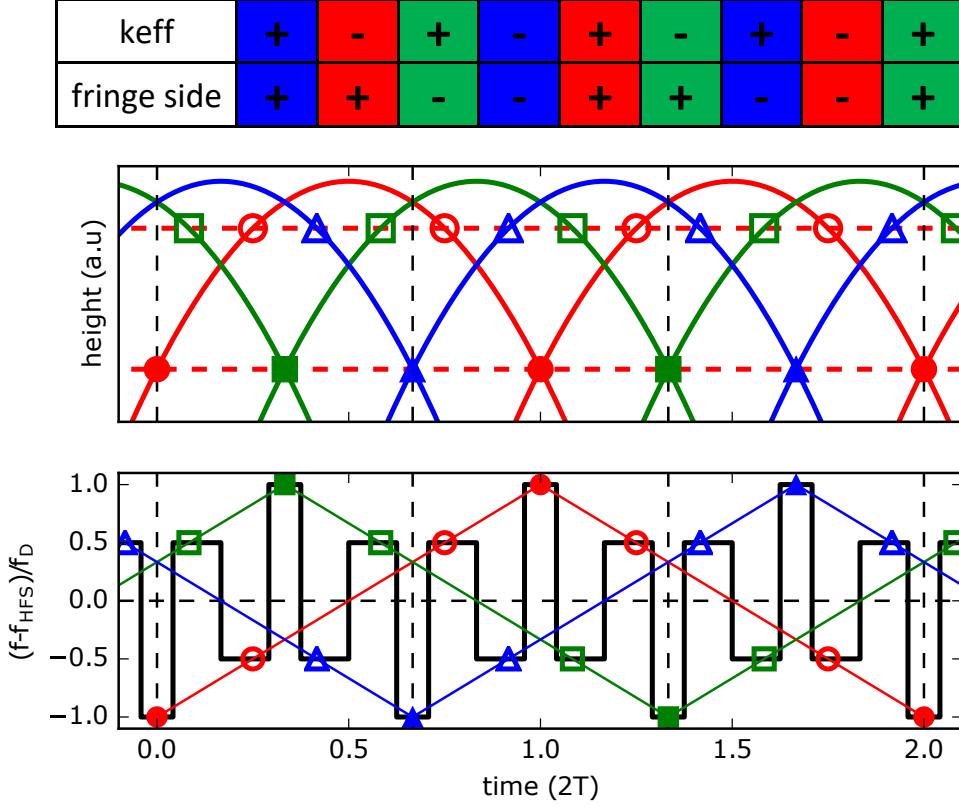


Figure 6: **Details of the sequence.** See the text for the explanations of the panels. In the bottom panel, $(f - f_{\text{HFS}})$ denotes the offset of the Raman laser relative frequencies from the hyperfine splitting frequency, and $f_{\text{D}} \simeq 611$ kHz the maximum Doppler effect, as defined in the Methods of the main text.

Fig. 6 shows the detail of the sequence. The top panel illustrates the alternation of the Raman wavevector ($\pm \vec{k}_{\text{eff}}$) and of the interferometer fringe side. The middle panel shows the height of the atomic cloud as a function of time (solid lines), thereby indicating the shared $\pi/2$ light pulses (solid symbols) and the not shared π light pulses (empty symbols). The color code highlights the joint points : successive sequences of the same color have one $\pi/2$ pulse in common. The bottom panel plots the correspond-

ing frequency difference of the Raman lasers (thick black line) to meet the two-photon resonance condition (thin colored lines, equivalent to a linear frequency ramp) at each shot. The symbols mark the light pulses.

Section S2: Raw data

Fig. 7 shows the raw data from which we extract the inertial phase shown in the main text. As written in Eq. (10), the total phase is computed as a sum of the SRS phase and of the atomic phase obtained from the transition probability. We extract the atomic phase by using a linear approximation of the response of the atom interferometer instead of the sinusoidal response, since we operate near the center of the fringe.

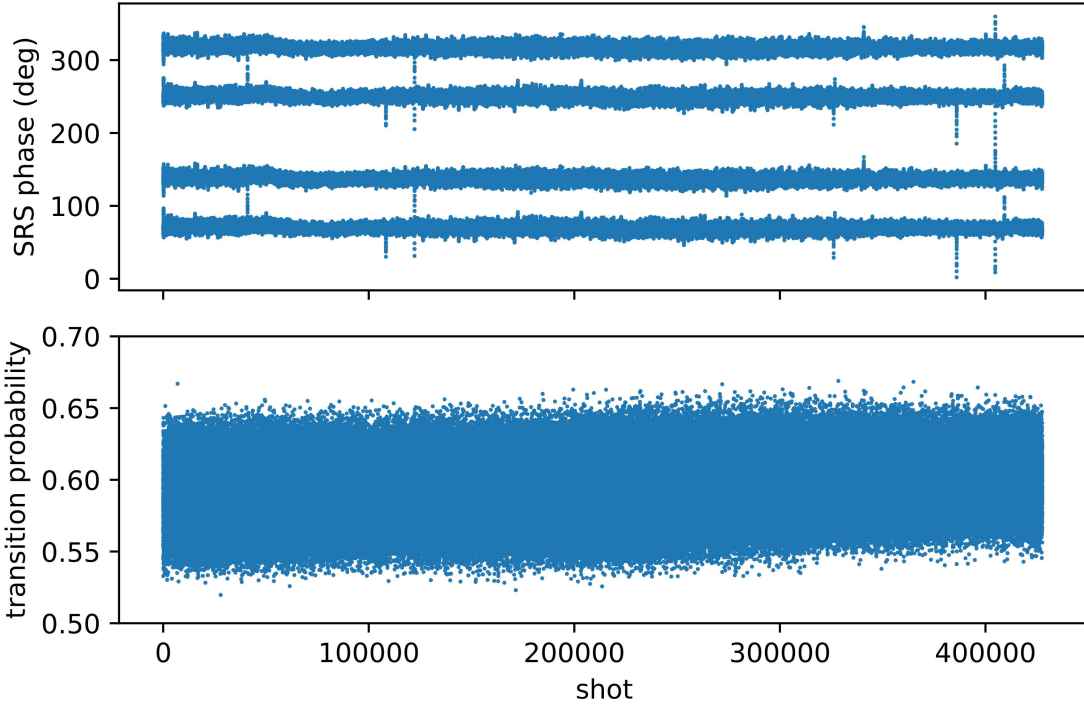


Figure 7: **Raw interferometer measurements corresponding to the data presented in Fig. 2 of the main text.** One shot corresponds to $T_c = 0.267$ s. The time axis spans from 21:10 on 23/09/2018 to 5:41 on 25/09/2018. The top panel shows the phase of the direct digital synthesizer (SRS) that is used to steer the interferometer at mid-fringe, for the four different configurations of interferometer ($\pm \vec{k}_{\text{eff}}$ and each with two sides of the fringe). The bottom panel shows the atomic transition probability, P , from which we extract the phase following Eq. (10) with $A \simeq 0.037$ the fringe amplitude.

Section S3: Analysis of vibration noise

Fig. 8 shows the amplitude spectral density of the linear acceleration noise of the experiment, $\sqrt{S_a(2\pi f)}$, recorded by the two seismometers. We estimate the contribution of each frequency band $[f_1 - f_2]$ to the interferometer phase noise by

$$\sigma_{\Phi}^2(f_1, f_2) = \int_{f_1}^{f_2} |H_a(2\pi f)|^2 S_a(2\pi f) df, \quad (11)$$

with $|H_a(2\pi f)| = \frac{8k_{\text{eff}}}{\omega^2} \sin(\frac{\omega T}{2}) \sin^2(\frac{\omega T}{4})$ the transfer function of the 4 pulse interferometer, see Ref. (42). This transfer function acts as a band-pass filter with a peak sensitivity centered around $1/T$. The result of the numerical integration in Eq. (11) is given in Table 1. The main contribution to the interferometer phase noise is the frequency band centered around 0.5 Hz. The estimation of the total phase noise (3.2 rad) with this method matches with the measured standard deviation of vibration phase (Fig. 5).

frequency band (Hz)	0.01-0.1	0.1-0.3	0.3-0.4	0.4-0.5	0.5-1	1-10	10-100	total
σ_{Φ}^2 (rad ²)	0.02	0.93	3.7	3.9	1.4	0.26	0.005	10.4

Table 1: Contribution of the linear acceleration noise to the interferometer phase noise by frequency band. The total rms phase noise is $\sigma_{\Phi} = 3.2$ rad.

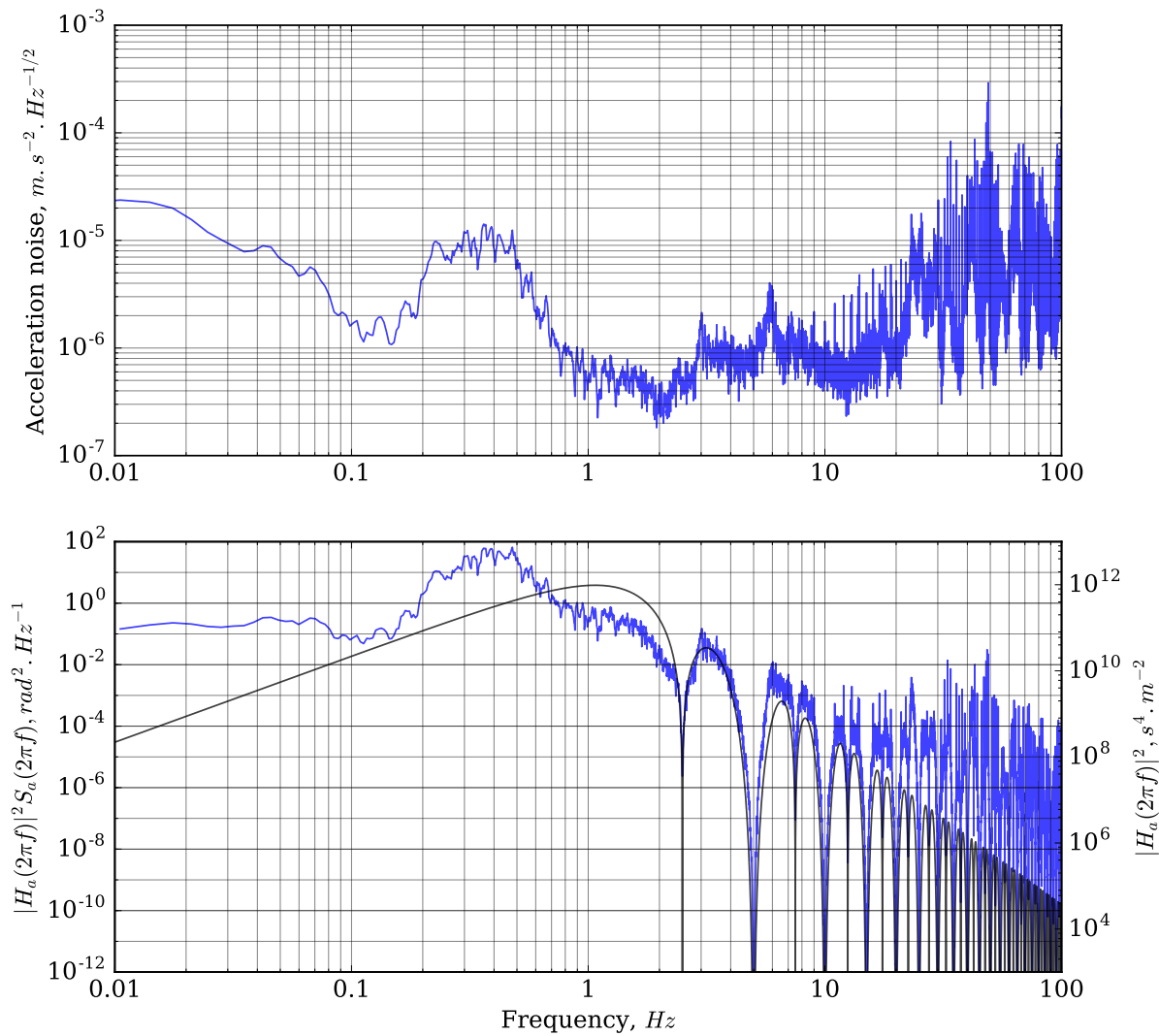


Figure 8: **Analysis of vibration noise.** Top: Amplitude spectral density of linear acceleration noise. Bottom: contribution to interferometer phase noise as from Eq. (11). The black line shows the acceleration transfer function of the interferometer, $|H_a(2\pi f)|^2$.

Section S4: Stability analysis

The stability of the gyroscope over the entire acquisition displayed in Fig. 2 of the main text is analyzed in Fig. 9. As the data set includes the day time where the vibration noise is higher than during night time, the short term sensitivity is slightly worse than in Fig. 3 of the main text, but the τ^{-1} scaling is still clearly visible.

When looking closely at the raw data averaged over 267 s segments (orange trace in Fig. 2 of the main text), a small modulation can be noticed. To highlight it, we show in the inset of Fig. 9 the result of a sinusoidal fit to the 267 s averaged data where the fit period is fixed to 24 hours; the fitted amplitude equals 4.0 mrad. This sinusoidal modulation reveals itself as a drift of the Allan deviation around 10 000 seconds, at the level of about $0.5 \text{ nrad}\cdot\text{s}^{-1}$. We attribute this modulation to a daily variation of the relative angle between the Raman beams in the y direction: as explained in the Material and Methods (section 'Alignment of the two Raman beams and atom trajectory'), a drift of $0.2 \mu\text{rad}$ is enough to explain a modulation of 4.0 mrad of the interferometer phase. Removing this instrumental drift yields the orange trace in Fig. 9, showing a stability of $3 \times 10^{-10} \text{ rad}\cdot\text{s}^{-1}$ at 30 000 s integration time, in agreement with that read from Fig. 3 of the main text for a shorter integration time.

Section S5: Analysis of the dynamic rotation rate measurements

Following Eq. 1 of the main text and Ref. (34), the full phase shift in our atom interferometer can be expressed as

$$\Phi = \frac{1}{2} \vec{k}_{\text{eff}} \cdot (\vec{\Omega}_E \times \vec{g}) T^3 + \frac{3}{4} \vec{k}_{\text{eff}} \cdot (\vec{\Omega}_F \times \vec{g} + \vec{\Omega}_E \times \vec{a} + \vec{\Omega}_F \times \vec{a}) T^3, \quad (12)$$

with $\vec{\Omega}_E$ the Earth rotation rate, \vec{g} the local acceleration of gravity, $\vec{\Omega}_F$ the rotation rate of the experimental apparatus with respect to the local geostationary reference frame,

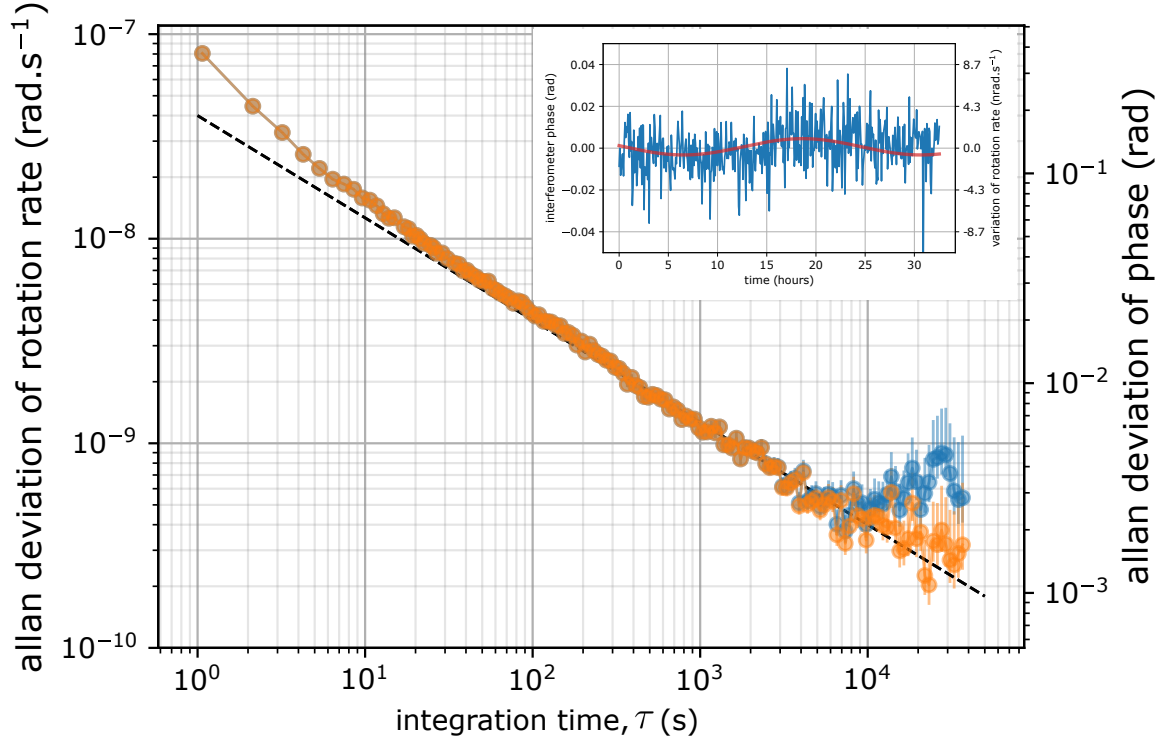


Figure 9: **Stability analysis of the gyroscope.** Blue: Allan deviation of the rotation rate measurement of Fig. 2 of the main text. Orange: Allan deviation of the measurement when subtracting a fitted sinusoidal modulation of fixed 24 hour period (inset). The dashed line is a visual guide to the eye representing a scaling as $4 \times 10^{-8} \text{ rad.s}^{-1} \times \tau^{-1/2}$.

and \vec{a} the acceleration of the apparatus with respect to that frame. For the demonstration of dynamic rotation rate measurements presented in the main text (Fig. 4), the rotation rate of the apparatus is modulated as $\vec{\Omega}_F(t) = \Omega_0 \cos(\omega t) \hat{u}_y$, the Earth rotation phase shift (first term in Eq. (12)) is a constant offset, and the two terms in the second parenthesis involving the acceleration \vec{a} of the apparatus are negligible. Therefore the dynamical phase shift reads

$$\Phi_{\text{dyn}}(t) \simeq \frac{3}{4} \vec{k}_{\text{eff}} \cdot (\vec{\Omega}_F(t) \times \vec{g}) T^3 = \mathcal{S} \Omega_F(t), \quad (13)$$

with $\mathcal{S} = \frac{3}{4}k_{\text{eff}}gT^3$. This expression is valid if the rotation rate is constant over the duration of the interferometer ($2T = 801$ ms). Here, we apply sinusoidal modulations of $2\pi/\omega = 5 - 10$ s period, and the atom interferometer delivers at every shot iT_c a rotation signal integrated over a duration of $2T$:

$$\Phi(iT_c) = \mathcal{S}\Omega_0 \cos[\omega(iT_c + T)] \times \frac{\sin(\omega T)}{\omega T}. \quad (14)$$

The last term corresponds to a correction of 0.96 for 5 s period, and 0.99 for 10 s period. To reconstruct the total phase from the atom interferometer, we sum the contribution of the phase deduced from the transition probability, P_i/A (with A the fringe amplitude), and the phase $\Phi_{\text{RTC},i}$ which was used in the real time compensation.

To compare the amplitude of the signal measured on the atom interferometer with the expected signal amplitude, we need to know accurately the applied rotation rate amplitude $\Omega_0 = \omega\theta_0$. Here θ_0 is the amplitude of the applied sinusoidal modulation of the orientation of the experiment, as defined in the main text. We measure θ_0 by comparing the signal of three different sensors: a tiltmeter, an accelerometer (which is sensitive to the the projection of gravity on its horizontal axis, $g \sin \theta_x(t) \simeq g\theta_x(t) = g\theta_0 \sin(\omega t)$), and a seismometer (which is sensitive to the integrated projection of gravity). Taking into account the calibrated response of these instruments, we extract θ_0 and find an agreement between the three sensors with a relative discrepancy of 5%. This allows us to calculate the amplitude of the sinusoidal signal in Eq. (14), $\mathcal{S}\omega\theta_0 \times \frac{\sin(\omega T)}{\omega T}$, with an uncertainty of 5%. The measured amplitude agree with the expected amplitude within this uncertainty on θ_0 .

Section S6: Systematic effect from the scattered light

The light scattered by the MOT atoms, $P_{\text{sc}}(t)$, induces a differential light shift, $\delta_{\text{AC}}(t) \propto P_{\text{sc}}(t)$, which, when integrated over time along the trajectories of the atoms in the in-

terferometer, results in a phase shift, $\phi_{AC} \propto \int P_{sc}(t)dt$. The induced light shift is largely canceled by the symmetric, spin-echo-like, four pulse configuration, and by the use of \vec{k}_{eff} reversal. Still, to measure any possible residual effect from the scattered light on the inertial signal, we vary the MOT loading time from $t_1 = 35$ ms to $t_2 = 55$ ms. On such timescales, we observe that $P_{sc}(t) \propto t$ by recording the MOT fluorescence, which corresponds to a scaling of the induced light shift $\phi_{AC} \propto t^2$.

When varying the loading time from t_1 to t_2 , we measure a non-inertial contribution (obtained from the half-sum of \vec{k}_{eff} measurements) of (55 ± 16) mrad, in agreement with a calculation of the expected light shift contribution. On the inertial signal (obtained from the half-difference of \vec{k}_{eff}), the measured phase difference is (20 ± 17) mrad. Since $\phi_{AC} \propto t^2$, varying the loading time from t_1 to t_2 amounts to vary the systematic shift by a relative factor $[(t_2 - t_1)/t_2]^2 \simeq 60\%$, with respect to the effect associated to the usual $t_2 = 55$ ms loading time. Our measured fluctuations of 1% rms of the level of scattered light (for 55 ms MOT loading time) thus translate into an upper bound on the phase instability of $20 \text{ mrad} \times \frac{1}{60} \simeq 0.3 \text{ mrad}$, corresponding to a gyroscope instability of $7 \times 10^{-11} \text{ rad.s}^{-1}$ (we translate phase to rotation rate using the scale factor of Eq. 2 of the main text). The influence of the scattered light from the fluorescence detection was evaluated to be even lower.